Insights from scanning tunneling microscopy experiments into correlated electron systems

Benschop, T.

Citation

Benschop, T. (2023, September 26). *Insights from scanning tunneling microscopy experiments into correlated electron systems*. *Casimir PhD Series*. Retrieved from https://hdl.handle.net/1887/3642190

Version:	Publisher's Version
License:	Licence agreement concerning inclusion of doctoral thesis in the Institutional Repository of the University of Leiden
Downloaded from:	https://hdl.handle.net/1887/3642190

Note: To cite this publication please use the final published version (if applicable).

Chapter 3

Measuring local moiré lattice heterogeneity of twisted bilayer graphene

We introduce a new method to continuously map inhomogeneities of a moiré lattice and apply it to large-area topographic images we measure on open-device twisted bilayer graphene (TBG). We show that the variation in the twist angle of a TBG device, which is frequently conjectured to be the reason for differences between devices with a supposed similar twist angle, is about 0.08° around the average of 2.02° over areas of several hundred nm, comparable to devices encapsulated between hBN slabs. We distinguish between an effective twist angle and local anisotropy and relate the latter to heterostrain. Our results imply that for our devices, twist angle heterogeneity has a roughly equal effect to the electronic structure as local strain. The method introduced here is applicable to results from different imaging techniques, and on different moiré materials.

This chapter has been published as T. Benschop, T. A. de Jong, P. Stepanov, X. Lu, V. Stalman, S. van der Molen, D. K. Efetov, and M. P. Allan, Measuring local moiré lattice heterogeneity of twisted bilayer graphene, *Phys. Rev. Research*, 3:013153, 2021

3.1 Introduction

Stacking two sheets of identical periodic lattices with a small twist angle θ leads to a super-periodic lattice with moiré lattice constant $\lambda(\theta)$ much larger than the original lattice constant a (figure 3.1a). This new lattice is called a moiré lattice. When using atomic layers exfoliated from van der Waals materials, and stacking them with a twist angle, the electronic and structural properties are modulated on the moiré length scale $\lambda(\theta)$, leading to the potential for new, emergent electronic properties of the moiré material [22, 73].

Such new properties have been spectacularly demonstrated in twisted bilayer graphene (TBG) around the magic angle of $\theta \approx 1.1°$ [20, 21, 74–80]. In TBG, the moiré lattice modulates the interlayer coupling between the individual graphene sheets, as well as the van der Waals forces on the individual carbon atoms. The former leads to flat bands of low-kinetic-energy electrons [22]. The latter leads to a slight deformation of the graphene lattice and bandgaps that separate the more localized electrons from the other bands [22]. When the flat bands are tuned to the Fermi level, they pair and condense into a superfluid at temperatures much higher than what one would naively expect at the low carrier densities observed in TBG [21]. Additionally, a variety of insulating and metallic behavior has been observed in TBG for different twist angles and band-fillings [20, 74, 75, 81].

The kinetic energy of the electrons changes rapidly as the twist angle is varied, especially around the magic angle, therefore the fabrication of devices with just the right angle is key in making them superconducting. But getting the right angle might not even be the most challenging aspect of fabricating high-quality superconducting TBG devices: contaminations, internal stress, and heterogeneities of the twist angle are difficult to avoid. This is in part because the magic angle is not the lowest energy configuration and in part because of the strong forces associated with the tear-and-stack technique. Internal stress and heterogeneities are often conjectured to limit the quality of the devices and are attributed as the main causes for the variability between devices [82]. This holds especially for open devices that lack the hBN top layer; notably such devices have never been found to superconduct. Measuring, visualizing, and characterizing heterogeneity in the twist angle and strain in TBG is thus crucial to understand and improve devices.

Probably the most complete visualization of inhomogeneity thus far has been obtained using scanning SQUID-on-tip microscopy (SOT) [83]. SOT measures the Landau levels as a function of location and thus has access to the local superlattice carrier density. On encapsulated devices, SOT has been used to visualize heterogeneity on length scales of a few micron with a resolution of several tens of nanometers, demonstrating that the twist angle varies by less than 4% [83]. While being a very precise measure of the local twist angle, SOT is also influenced by other factors, e.g. inhomogeneities of the chemical potential and the local magnetic screening. Other techniques to access homogeneity are Nano-ARPES [24, 84, 85], which can image the full electronic structure in reciprocal space with a spatial resolution of circa 600 nm, low energy electron microscopy (LEEM) [24], which can image structural inhomogeneities at twist angles lower and higher than the magic angle, conductive atomic-force microscopy

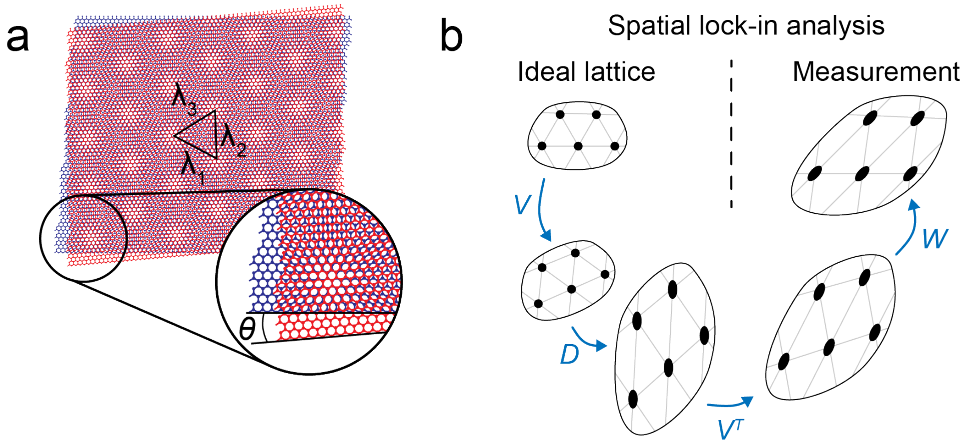

Figure 3.1: a) Moiré pattern created by stacking 2 hexagonal lattices with a twist angle of 5°. b) Schematic representation of our spatial lock-in algorithm to map the local twist angle and anisotropy. The measured lattice can be thought of as the result of a series of transformations applied to an ideal lattice. The scaling transformation, D, holds information about the local twist angle $\theta^*(\mathbf{r})$ and the intrinsic local strain present in the device, $\kappa(\mathbf{r})$. V gives the direction of this local strain, $\psi(\mathbf{r})$. Finally, W indicates the relative angle between the bilayer and the underlying hBN substrate.

(AFM) [86], nano-photocurrent mapping [87], which can measure the twist angle with a resolution on the order of 20 nm, and scanning single electron transistors [88], which can map the twist angle by measuring the inverse local compressibility. Finally, scanning tunneling microscopy (STM), the probe used in this study, has been used to measure both the topography and the local density of states of TBG, including the emergence of correlations at the magic angle [89–94].

In previous STM studies, two different methods have been used to determine the local twist angle. First, one can determine the twist angle using three neighboring moiré lattice sites in real space. The distances between each lattice site, $\lambda_1, \lambda_2, \lambda_3$ are fit to a set of equations that yield the twist angle at a per-triangle resolution (figure 1a) [90], and, using a model with assumptions about the strain distribution in the two layers, an estimate for the heterostrain ϵ.

A second method to determine the twist angle uses the Fourier transform of a real space topography to determine the moiré wavelengths λ_j in the three directions of the moiré lattice (in principle, two directions are fully determining the lattice, but often all three are used for a better signal-to-noise ratio). The twist angle is determined using $\lambda = \frac{a}{2\sin(\frac{\theta}{2})}$, where $\lambda = \frac{1}{3}\sum_{j=1}^{3}\lambda_j$ and a is the lattice constant of graphene. Using the Fourier transform is generally more accurate than fitting three moiré lattice peaks, because it averages over the whole field of view, but this also limits its spatial resolution to the full field of view.

In this work, we introduce an alternative method of quantifying and visualizing the heterogeneity in open devices, with sub-moiré lattice cell resolution over length scales of hundreds of nanometers. We develop a spatial lock-in method that enables one to map, with sub-moiré wavelength resolution, the local twist angle $\theta^*(\mathbf{r})$, the local moiré anisotropy $\kappa(\mathbf{r})$, and the anisotropy direction $\psi(\mathbf{r})$, as defined below. Notably, we can separate these effects from each other and from rotations of the lattice (figure 3.1b). We then apply our method to determine the heterogeneity in open TBG devices.

3.2 Methods

We fabricate our devices using the tear and stack method with a special focus on avoiding contamination to ensure the large clean areas needed for this study. A single graphene flake is pre-cut in halves with an AFM tip, ensuring initial crystallographic alignment between them. The first half is subsequently picked up with a hBN flake, mechanically exfoliated on a SiO_2/Si chip and adhered to a PDMS/PC stamp at ~ 100 °C. The second half of graphene is manually rotated to a target twist angle of $1.5°$–$2.0°$ and consequently picked up by the hBN/graphene stack on PC. In the next step, the PC layer is carefully peeled off of the initial PDMS stamp and placed on another PDMS stamp up-side down. The sacrificial polycarbonate (PC) layer is then removed in 1-Methyl-2-Pyrrolidone. Subsequently, the TBG/hBN heterostructure is transferred on a target SiO_2/Si substrate with a pre-patterned navigation structure, two gold electrodes and a graphite gate contacting one of them within the measurement area. We carefully align the TBG/hBN stack with the local graphite gate to avoid short circuiting. The second pre-patterned gold electrode is used to electrically contact TBG using another graphite piece. The devices are inserted into our ultra-high-vacuum setup and annealed at 350°C for 12h before inserting them into the low-temperature STM operating at 4.2K. The TBG samples are located using a capacitive navigation scheme [95].

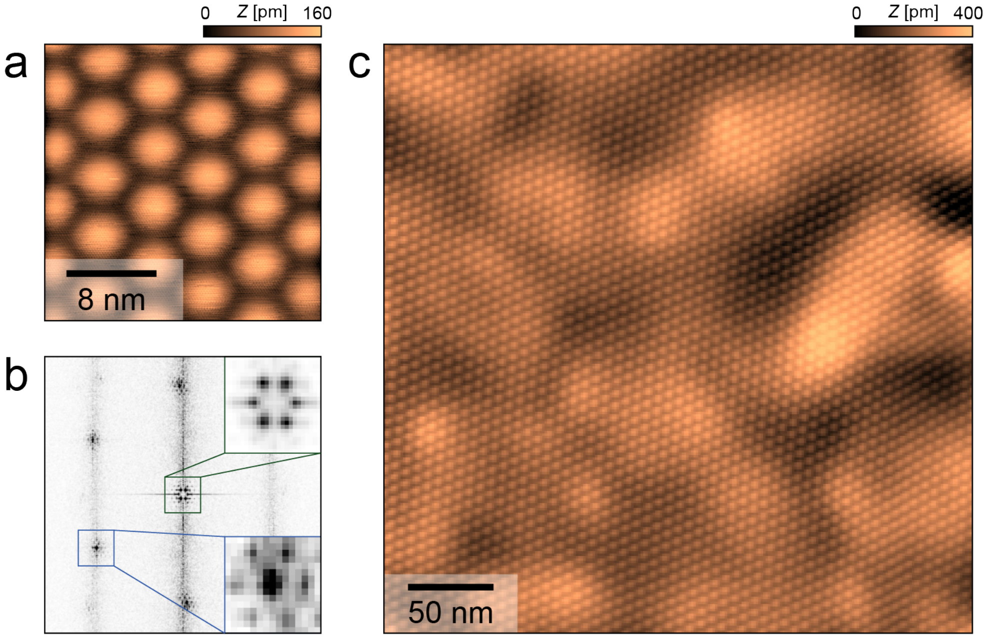

Figure 3.2: a) STM topography of a device with an average twist angle of $\theta = 2.38°$ (set-up conditions: V = 250 mV, I = 100 pA). The topography shows both the atomic- and moiré lattice. b) Fourier transform of a, with zoom ins of the moiré peaks (green inset) and the bottom left atomic peak (blue inset). Satellite peaks of the moiré lattice are visible around the atomic peak as well. c) Large scale topography measured on a different device with an average twist angle of 2.02° (set-up conditions: V = 250 mV, I = 20 pA).

3.3 Spatial lock-in algorithm

Figure 3.2a shows a topographic image where both the atomic lattice of the top graphene layer and the moiré lattice are resolved. The Fourier transform of the image shows the lattice peaks as well as the peaks from the moiré superlattice (figure 3.2b, blue and green inset respectively). While such small field-of-views are well suited for spectroscopy studies, we require large field of views that encompass many moiré cells for the heterogeneity study using spatial lock-in detection presented here. Figure 3.2c shows an example.

The general method of spatial lock-in is illustrated in figure 3.3 for the one-dimensional case: the "measured" signal $S(x)$, a not-quite periodic signal, is multiplied with a reference signal, a perfectly periodic complex plane wave $S_{ref}(x)$. The phase of the resulting signal, when low pass-filtered, corresponds to the local phase of the original wave. To obtain the local variations in wavelength $\lambda(x)$ of the original wave, shown on the bottom, one calculates the derivative of the local phase. Spatial lock-in algorithms like this have been used previously in electron microscopy studies (known as geometric phase analysis) [96–98] and optical metrology [99]. In the context of STM, the most well-known application is known as the Lawler-Fujita algorithm [100]. Lawler, Fujita et al. have, based on earlier work by Slezak et al. [101], introduced a lock-in algorithm to correct topographic images for drift by calculating the displacement field, i.e. the vectors that connect the coordinates of the measured images with the points of an ideal reference lattice. Our motivation here is different: we do not need to correct an imperfect image, but want to extract heterogeneities of the lattice.

To do so, we start with defining three reference plane waves $R_j(\mathbf{r}) = e^{i\mathbf{q}_j\cdot\mathbf{r}}$, $j \in \{1,2,3\}$, where the reference wavevectors q_j are determined by simultaneously fitting six gaussians to the Bragg peaks in the Fourier transform of the topography (figure 3.4b). In order to measure deviations from an isotropic triangular lattice, we force the reference wavevectors to be of equal magnitude and 60 degrees with respect to each other (although see appendix B.1.4 on choice of reference vectors). The reference lattice is then defined as the real part of the sum of the reference plane waves, i.e. $T_r(\mathbf{r}) = \mathrm{Re}\left[T_0 \sum_j R_j(\mathbf{r})\right] = T_0 \sum_j \cos(\mathbf{q}_j \cdot \mathbf{r})$, where T_0 is the average amplitude.

The transformation between the measured lattice, $T_m(\mathbf{r})$, and this perfectly periodic, hexagonal reference lattice, $T_r(\mathbf{r})$ can approximately be parametrized as the shifts between points in the moiré lattice and corresponding points in the reference lattice. To this end, we introduce the displacement field, $\mathbf{u}(\mathbf{r})$, in the following manner:

$$T_m(\mathbf{r}) = T_r(\mathbf{r} + \mathbf{u}(\mathbf{r})) = T_0 \sum_j \cos\left(\mathbf{q}_j \cdot (\mathbf{r} + \mathbf{u}(\mathbf{r}))\right). \tag{3.1}$$

To extract the displacement field from our data, each reference signal is multiplied with the original topographic image and low-pass filtered with a gaussian window. This operation corresponds to convolution of the original topographic image with the plane wave encompassed by a gaussian, calculating the relevant wave vector component of the ultimately small window 2D Fourier transform. The window of the gaussian filter needs to be chosen large enough (small enough in frequency space), in order to exclude

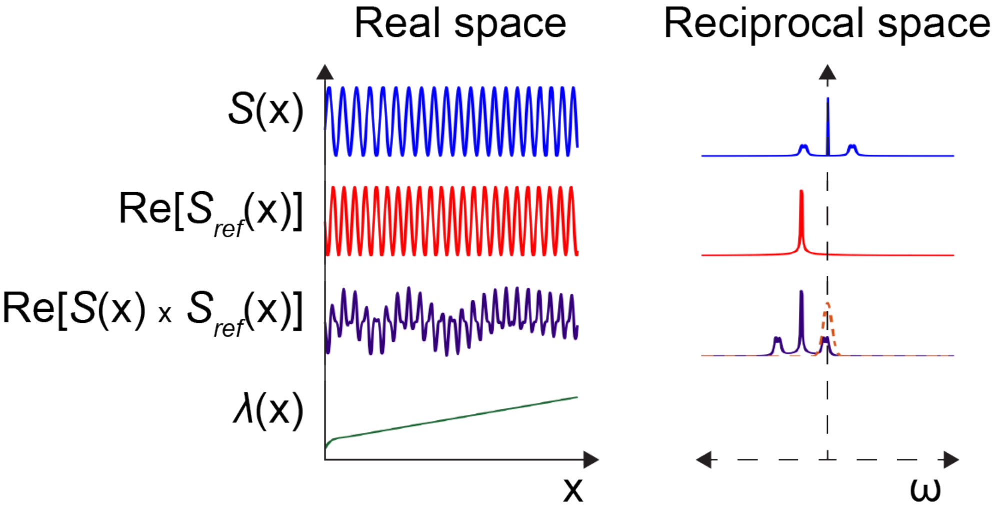

Figure 3.3: Lock-in in 1D. The panels in the left column show, from top to bottom, the signal (an almost periodic sinusoid), the real part of the reference, the real part of the product of the signal and reference, and the wavelength calculated by taking the gradient of the phase of the product signal. The right column displays the Fourier transform of the (complex) signals in the left column. Finally, in the bottom right curve, the orange dashed line represents the gaussian filter used for the lock-in procedure.

larger frequencies, but simultaneously small enough (big enough in frequency space) to maintain good spatial resolution (appendix B.1). A lower limit on the filter size is put in place by higher frequencies: If the filter is chosen too small (too large in frequency space), more higher frequencies become included in the filter window reducing the signal to noise ratio. In practice a filter width of a few periods is used, as illustrated by the circle in figure 3.4a. The local phase of the result of this operation corresponds to the local shift between the real image and the reference wave, or more precisely $\phi_j(\mathbf{r}) = \mathbf{q}_j \cdot \mathbf{u}(\mathbf{r})$ (appendix B.1).

This local phase is 2π periodic and needs to be phase-unwrapped to remove discontinuities. After phase unwrapping, the displacement field $\mathbf{u}(\mathbf{r})$ can be extracted from two of the phase maps by pixel-wise multiplication with Q^{-1}, the inverse of a matrix containing the used wave vectors (Although not applied here, using all three wave vectors is more involved but can be beneficial for low signal-to-noise ratio situations, as detailed in appendix B.1.4).

In a second step, we decompose the obtained displacement field, $\mathbf{u}(\mathbf{r})$ into the local effective twist angle, $\theta^*(\mathbf{r})$ and the local moiré anisotropy magnitude and direction, $\kappa(\mathbf{r})$ and $\psi(\mathbf{r})$ respectively. To that end, we consider the Jacobian of the transformation, $J = I + \nabla\mathbf{u}$, which is the displacement gradient tensor that describes the transformation of an infinitesimal triangle at each position. The polar decomposition $J = WA$ splits J into the product of the unitary matrix W, describing the local rotation of the lattice and a matrix A, describing the local scaling and anisotropy. This matrix A can be further decomposed into a (unitary) rotation matrix V, indicating the major and minor axis of scaling and a diagonal scaling matrix D such that $J = WA = WV^T DV$. This final decomposition is illustrated in figure 3.1b and makes it straightforward to extract relevant quantities. The change in density of unit cells is equal to the change in area under the effect of the deformation gradient tensor, hence the geometric mean of the scaling elements in the diagonal of D, $\sqrt{d_1 d_2} = \sqrt{\det(J)}$, allows us to calculate the wavelength of the moiré lattice and consequently, the local twist angle (appendix B.1). Furthermore, the local anisotropy magnitude, $\kappa(\mathbf{r})$, is calculated by taking the ratio of the scaling elements that make up D, $\kappa = \frac{d_1}{d_2}$, where $d_1 > d_2$. Defined in this way, $\kappa = 1$ indicates an isotropic lattice, and $\kappa > 1$ indicates an anisotropy of the moiré lattice in the direction given by ψ, the angle corresponding to the rotation corresponding to V. Lastly, the rotation of the total lattice, corresponding to W, is left unattended, as a rotation of the full lattice should not directly influence the physics at play, although we point out that it does describe the variations of the rotation with respect to the hBN substrate.

3.4 Results

Figure 3.4c shows the effective twist angle $\theta^*(\mathbf{r})$, figure 3.4d the local anisotropy $\kappa(\mathbf{r})$ and figure 3.4e shows the angle of major scaling $\psi(\mathbf{r})$, all as a function of location for open-device TBG. The maps show rather smooth variations with an exception in the bottom right corner of the field of view, where an apparent vertical feature appears. This feature is only barely visible in the topography itself, showcasing the sensitivity of our method. The origin of this particular vertical stripe remains unclear, and no such peculiarities were observed in our other data (appendix B.7).

The overall twist angle heterogeneity in the image in figure 4c, excluding border effects, is 0.033° (standard deviation) or 0.23° peak-to-peak. We find areas of hundreds of nanometers with a standard deviation of the twist angle of 0.02° and a peak to peak variation of 0.08°, e.g. in the area marked by a red square in figure 4c. A good estimate of the accuracy of our method can be made by applying the conventional Lawler-Fujita algorithm [100] and using spatial lock-in to extract the residual displacement field (appendix B.5). We find residual twist angle variations more than one order of magnitude smaller than the originally found values, underlining the accuracy of our method. We further note that this is achieved with a pixel density corresponding to ∼5 pixels per moiré lattice constant, which makes implementation of the conventional heterostrain model challenging (appendix B.10).

Our result allows for a first comparison between open and encapsulated devices. For the latter, we compare our results with results from SOT [83]. SOT measures the superlattice density, $n_s(\mathbf{r})$, which scales directly with the size of the unit cell. We note that SOT does not differentiate between heterogeneity of the chemical potential, strain, and twist-angle, which can all influence $n_s(\mathbf{r})$.

To make a comparison between SOT and our data, one has to take into account the

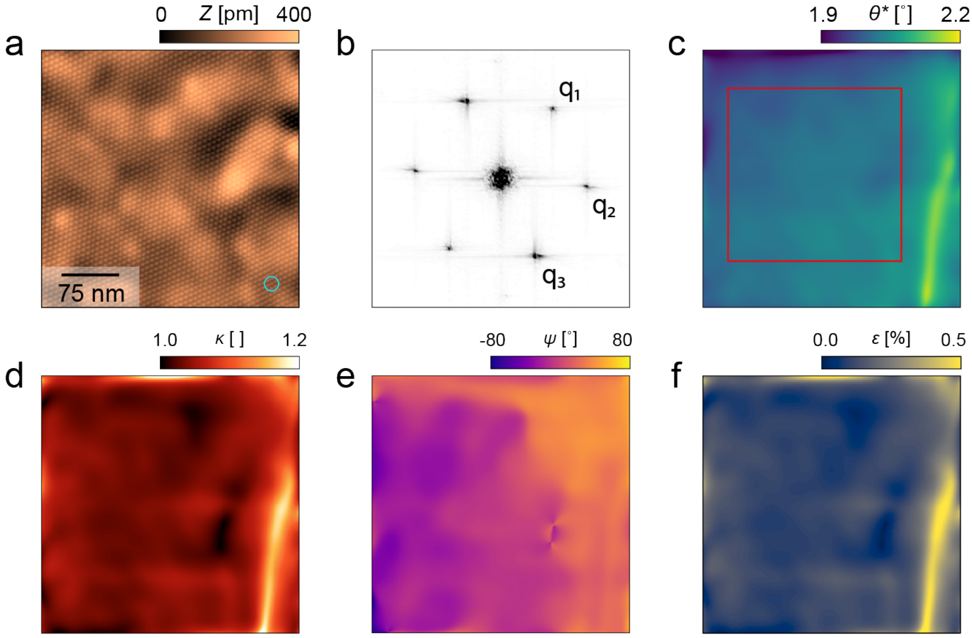

Figure 3.4: a) STM topography of a device with an average twist angle of 2.02° (V = 250 mV, I = 20 pA, same data as Figure 3.2c). The blue circle in the bottom right indicates the size of the filter used by the algorithm (see main text). b) Fourier transform of a, showing the Bragg peaks of the moiré lattice visible in the image. The Bragg peaks are labelled $q_1 - q_3$. c) Effective twist angle map extracted from a, by the algorithm discussed. The red square indicates the area over which the average twist angle and standard deviation are calculated. d) Local moiré anisotropy map $\kappa(\mathbf{r})$ extracted by the algorithm from a. e) Local moiré anisotropy direction $\psi(\mathbf{r})$ extracted by the algorithm from a. f) Heterostrain map extracted as described in the text.

difference in the width of the point spread function (PSF). As this width is around 30 nm for SOT, we artificially broaden the PSF of our data to match (appendix B.9), which naturally leads to a reduction of both the peak-to-peak spread and the standard deviation. In the full field of view, including the bright vertical feature, we find a peak to peak spread of 0.20° and a standard deviation of 0.036°. These numbers are similar among different devices of similar twist angle (appendix B.11) and measured for areas of several hundreds of nanometers across.

Interestingly, this result matches rather well with the result from SOT on encapsulated devices, despite the lack of a stabilizing top hBN slab in our devices. This implies that open devices can rival the quality of encapsulated devices, at least in terms of twist angle homogeneity.

Our results then raise the following question: why have open-devices never been shown to superconduct, nor to show spectral gaps in low temperature tunneling experiments? Assuming that the mechanical properties of the bilayer do not change drastically as the angle of reconstruction is approached ($\theta \approx 1.0°$), our experiments suggest that the homogeneity of the TBG itself cannot be the only reason. Instead, another reason might be the absence of a second hBN layer encapsulating the bilayer, despite hBN often being neglected in theoretical studies due to its supposed weak interaction. Furthermore, the second hBN layer creates a near symmetric environment for the bilayer. We speculate that breaking of this symmetry may be at the basis for the lack of superconductivity in open devices. However, more careful transport investigations of open devices are necessary to confirm this hypothesis.

The local anisotropy parameter $\kappa(\mathbf{r})$ discussed here can be related to heterostrain, following the model of Kerelsky et al. [90]. Here, it is assumed that one of the graphene sheets is strained with a uniaxial strain $\epsilon(\mathbf{r})$, while the other one is unaffected and only undergoes a rotation. To connect to our measurements, we note that for small average twist angles, the displacement field of the moiré lattice is related to relative displacement of the constituting layers by the following formula: $(\langle J\rangle - I)\cdot \mathbf{u}_{moir\acute{e}}(\mathbf{r}) = \mathbf{u}_{\downarrow}(\mathbf{r}) - \mathbf{u}_{\uparrow}(\mathbf{r}) = \mathbf{u}_{\sim}(\mathbf{r})$, where $\langle J\rangle$ is the Jacobian corresponding to the average angle between the layers and $\mathbf{u}_{\sim}(\mathbf{r})$ is the relative displacement field experienced between the two sheets (appendix B.2). The relative displacement field can be decomposed in the same way as before, where the angle corresponding to W now corresponds to the deviation of the twist angle between the two sheets from the average twist angle, and the local anisotropy $\kappa(\mathbf{r})$ and $\psi(\mathbf{r})$ obtained from the resulting scaling matrix indicate the relative strain between the layers. Furthermore, from the resulting scaling matrix elements, we can calculate the magnitude of the strain applied to the deformed sheet, $\epsilon(\mathbf{r})$ (appendix B.2). We show the resulting $\epsilon(\mathbf{r})$ in figure 3.4f. On average, we find that $\epsilon = 0.14\%$ with a standard deviation of 0.09%.

It is interesting to compare the numbers for strain and twist angle heterogeneity, and their respective influence on the electronic structure of TBG. Calculations using a continuum model have considered both strain and twist angle changes in TBG samples close to the magic angle [102]. It was shown that a heterostrain of $\epsilon \approx 0.1\%$ results in a splitting of the van Hove singularities of approximately 5 meV. This is comparable to variations in the twist angle of about 0.03°, which we obtain by interpolating the relation between twist angle and van Hove splitting given in [23]. Furthermore, stress can cause strong qualitative changes to the electronic structure including new van Hove singularities for $\epsilon \approx 0.5\%$. If we compare these numbers with our measurements, we conclude a roughly equal effect of the observed strain and twist angle inhomogeneity, suggesting that both have to be taken into account when fabricating samples, as both effects significantly alter the electronic structure compared to a perfect lattice.

Before concluding, we want to address one potential challenge of the method introduced here: it is also sensitive to piezo drift. Piezo drift occurs in STM experiments due to thermal fluctuations that influence the piezo, due to piezo relaxation after a change of field of view, or due to the piezo relaxation from the movement necessary to take the topography. The former two effects change over time. The latter effect depends on the speed with which the topography is measured. To check the validity of this procedure, we have repeated the above procedures for different topographies in the same field of view, taken with different scan speeds at different times. As we show in detail in appendix B.6, these different measurements yield very similar results, demonstrating that the twist angle variations we measure are intrinsic and not a consequence of piezo drift.

3.5 Conclusion

In this work, we have visualized and characterized structural heterogeneity in TBG, demonstrating peak to peak variations in the twist angle of roughly 0.08° over areas of hundreds of nanometers. While our samples exhibit an average twist angle higher than the magic angle, we expect the issues to be similar as long as the twist angle is above the reconstruction that occurs for twist angles $\lesssim 1^\circ$. This indicates that the best open device TBG could, purely based on homogeneity of the twist angle, superconduct, and that lack of experimental evidence thereof suggests a critical role of the missing hBN top layer. The spatial lock-in algorithm we introduced is in principle applicable to a variety of different moiré materials, and additionally, may also be usable in a different context, e.g. in determining the topological properties of band structures through QPI measurements [103]. We anticipate that this algorithm can be applied to other microscopy probes as well, including AFM and LEEM. Lastly, by presenting our results in the way we did, we hope to pave the way for further studies, especially for correlating electronic- and spatial properties by combining with theoretical models like the ones presented in references [102, 104, 105].